

# Hierarchical tubular MoP/MoS<sub>2</sub> composite with enhanced electrochemical hydrogen evolution activity

**Peiyuan Wang**

Zhengzhou University of Light Industry

**Xiaoqian Wang**

Zhengzhou University of Light Industry

**Renyi Diao**

Zhengzhou University of Light Industry

**Yujie Guo**

Zhengzhou University of Light Industry

**Yuxiang Wang**

Zhengzhou University of Light Industry

**Chao Zhou**

Zhengzhou University of Light Industry

**Ke-Feng Xie**

Lanzhou Jiaotong University

**Shumin Sun** (✉ [smsun@zzuli.edu.cn](mailto:smsun@zzuli.edu.cn))

Zhengzhou University of Light Industry <https://orcid.org/0000-0002-5385-0434>

**Yong-Hui Zhang**

Zhengzhou University of Light Industry

---

## Research Article

**Keywords:** MoP/MoS<sub>2</sub>, heterojunction, hierarchical, tubular, hydrogen evolution reaction

**Posted Date:** February 24th, 2021

**DOI:** <https://doi.org/10.21203/rs.3.rs-225827/v1>

**License:**   This work is licensed under a Creative Commons Attribution 4.0 International License.

[Read Full License](#)

---

# Abstract

Electrocatalytic production of hydrogen from water is a promising and sustainable strategy. Herein, hierarchical tubular MoP/MoS<sub>2</sub> composites with the wall composed of loosely stacked nanosheets were fabricated through partially phosphating the tubular MoS<sub>2</sub>. As an electrocatalyst for hydrogen evolution reaction (HER), the hierarchical tubular MoP/MoS<sub>2</sub> composite displayed a superior HER activity with a low overpotential (101 mV) to obtain a current density of 10 mA/cm<sup>2</sup>, small Tafel slope (56 mV/dec). Moreover, the MoP/MoS<sub>2</sub> composite demonstrate superior long-term durability in acid electrolytes. The excellent catalytic activity of MoP/MoS<sub>2</sub> composite may be ascribed to its hierarchical structure: hierarchical porous structure can offer mass diffusion pathways, and the nanosheets with MoP/MoS<sub>2</sub> heterojunctions can provide rich active sites for HER. Density functional theory (DFT) calculations reveal that more favorable H\* adsorption kinetics on the surface of the MoP/MoS<sub>2</sub> composite during the HER process than pristine MoP and MoS<sub>2</sub>. This work can offer a strategy to design high performance electrocatalysts for HER applications.

## Introduction

Due to its renewability, environmental friendliness, and highest mass-specific energy density, hydrogen has been recognized as the promising alternative to fossil fuel [1]. Among the hydrogen production approaches, the electrocatalytic water splitting using electrical energy is believed to be a safe and efficient process [2]. Currently, Pt-group metals have been proved to be the state-of-the-art electrocatalyst towards Hydrogen evolution reaction (HER) [3]. However, their high cost and low earth-abundance hinder the scale-up application. Therefore, it is necessary to develop the cost-effective electrocatalysts that drive HER with high reaction rate at low overpotential.

Due to the low-cost and earth-abundance, metal oxides have been intensively studied as good candidates for HER electrocatalysis. Various strategies, such as morphology engineering, oxygen-vacancy control, phase structure engineering and non-metal or metal doping have been adopted to enhance the metal oxides electrocatalytic performance [4]. Besides of the metal oxides, metal chalcogenides and phosphides, such as MoS<sub>2</sub> [5], WSe<sub>2</sub> [6], CoP [7], MoP [8] and Ni<sub>2</sub>P [9], have generated great interest for their catalytic activity toward HER. Among them, two-dimensional (2D) MoS<sub>2</sub> has been investigated as the most potential alternative to Pt-based HER catalyst [10]. Both theoretical and experimental studies have illustrated that the exposed edges of MoS<sub>2</sub> were active sites for HER [11]. However, the low conductivity and limited exposed active sites of 2D MoS<sub>2</sub> hinder its practical application. So far, several strategies were applied to enhance the HER activity of MoS<sub>2</sub>, such as, fabricating nanostructure MoS<sub>2</sub> to increase the active sites [12-14], doping transition metals in MoS<sub>2</sub> to increase the intrinsic catalytic activity [15,16], or coupling with conductive substrates to increase the conductivity [17,18].

Besides MoS<sub>2</sub>, MoSe<sub>2</sub> [19], MoP [8], Mo<sub>2</sub>C [20], MoN [21], and MoO<sub>2</sub> [22] also exhibit catalytic performance of HER. In addition, the Mo-based composites, such as MoS<sub>2</sub>/MoSe<sub>2</sub> [23], MoP/Mo<sub>2</sub>C [24],

MoN/Mo<sub>2</sub>C [25] and MoP/MoS<sub>2</sub> [26-28] displayed excellent HER activity due to the synergistic effect. Especially MoP/MoS<sub>2</sub> composites have been studied a lot due to their high electrocatalytic activity. For example, MoS<sub>2</sub>(<sub>1-x</sub>)P<sub>x</sub> (x=0 to 1) solid solution prepared by annealing bulk particulate MoS<sub>2</sub> with red phosphorus needed an overpotential of  $\approx 150$  mV to deliver a current density of 10 mA cm<sup>-2</sup> [29]. The hierarchical MoS<sub>2</sub>@MoP core-shell heterojunction electrocatalysts exhibited excellent electrocatalytic activity for HER with a low onset overpotential of 29 mV and  $\eta$  of 108 mV at 10 mA cm<sup>-2</sup> in 0.5 M H<sub>2</sub>SO<sub>4</sub> and retains its good activity for 30 h [30]. In addition, the catalyst showed excellent activity in 1 M KOH with an onset overpotential of 42 mV and  $\eta$  of 119 mV at 10 mA cm<sup>-2</sup>. The MoP/MoS<sub>2</sub> nanosheets on carbon cloth only needed a low overpotential of 96 mV to achieve a current density of 10 mA cm<sup>-2</sup> for HER in the neutral medium, ascribing to plentiful active sites on the heterointerface of MoP/MoS<sub>2</sub>, good conductivity of MoP and CC for electron transfer, and pores surrounded by MoP/MoS<sub>2</sub> nanosheets [31]. Due to the synergistic effect of MoP and MoS<sub>2</sub>, most of the MoP/MoS<sub>2</sub> composites show extraordinary electrochemical properties.

Considering the electrochemical performances of the electrode material are associated with transportation of electrolyte and electrochemical reaction, a hierarchical hollow nanostructure will be benefit for their electrochemical properties [32,33]. In addition, the two-dimensional (2D) nanosheet can provide rich accessible active sites, so a hierarchical porous structure catalyst composed of MoP/MoS<sub>2</sub> nanosheets with rich heterojunctions may be a superior electrocatalyst for HER.

Based on the above consideration, a hollow tubular MoS<sub>2</sub> with the wall composed of nanosheets was prepared. Using it as template, a series of MoP/MoS<sub>2</sub> composites were fabricated through partially phosphating the tubular MoS<sub>2</sub>. In the obtained MoP/MoS<sub>2</sub> composites, besides of the inherited hollow tubular, nanosheet structure from MoS<sub>2</sub>, the rich heterojunctions between MoP and MoS<sub>2</sub> can be found. As HER electrocatalyst, MoP/MoS<sub>2</sub>-1 displayed a superior HER activity with an onset potential about 37 mV and an overpotential of 101 mV to obtain a current density of 10 mA/cm<sup>2</sup>, and the Tafel slope was 56 mV/dec. The superior catalytic activity of MoP/MoS<sub>2</sub>-1 may be ascribed to its hierarchical structure: hierarchical porous structure can offer mass diffusion pathways, the nanosheets with MoP/MoS<sub>2</sub> heterojunctions can provide rich active sites for HER.

## Experimental Section

### *Synthesis of tubular MoP/MoS<sub>2</sub> heterostructure*

The tubular MoP/MoS<sub>2</sub> composites were prepared by partially phosphating of tubular MoS<sub>2</sub> (Scheme 1). Firstly, tubular MoS<sub>2</sub> was prepared through a hydrothermal method in a 100 mL Teflon-lined autoclave at 200 °C for 6 h using (NH<sub>4</sub>)<sub>6</sub>Mo<sub>7</sub>O<sub>24</sub>•4H<sub>2</sub>O, thioacetamide (TAA), and tetramethylammonium bromide (TMAB) as raw materials [34]. Secondly, MoP/MoS<sub>2</sub> composites were prepared by phosphating the as-prepared tubular MoS<sub>2</sub>. Typically, 100 mg MoS<sub>2</sub> and 100 mg NaH<sub>2</sub>PO<sub>2</sub> were separately placed in two

ceramic boats, then the boats were put in an alumina tube. The samples were calcinated in the tubular furnace with  $\text{NaH}_2\text{PO}_2$  at the upstream side in a sealed system under Ar atmosphere at 800 °C for 2 h. The total reactive mechanism is as follows: [35]

The product was denoted as  $\text{MoP}/\text{MoS}_2$ -1. In order to adjust the phosphidation degree of the  $\text{MoS}_2$ , a series of weight ratio of  $\text{NaH}_2\text{PO}_2$  to  $\text{MoS}_2$  were placed in the furnace, and the products were denoted as  $\text{MoP}/\text{MoS}_2$ -x, where x represents the weight ratio of  $\text{NaH}_2\text{PO}_2$  to  $\text{MoS}_2$ .

### ***Characterization methods***

Powder X-ray diffraction (XRD) patterns of the prepared samples were conducted on a Bruker D8 Advance X-ray diffractometer equipped with  $\text{Cu K}\alpha$  ( $\lambda=1.5418 \text{ \AA}$ ). The morphologies of the prepared samples were investigated with scanning electron microscopy (SEM, JSM-6490LV), field emission scanning electron microscope (FESEM, JSM-7001F) and transmission electron microscopy (TEM, JEM-2100). The X-ray photoelectron spectroscopy (XPS) was recorded on a Thermo Scientific ESCALab 250Xi photoelectron spectrometer equipped with a monochromatic  $\text{Al K}\alpha$  source ( $\lambda=1486.7 \text{ eV}$ ).

### ***Electrochemical measurements***

Electrochemical measurements were performed in a typical three-electrode setup in 0.5 M  $\text{H}_2\text{SO}_4$  on a CHI 660E electrochemical workstation. The prepared  $\text{MoP}/\text{MoS}_2$  composites coated on the glass carbon electrode (GCE), a saturated calomel electrode (SCE) and a graphite rod were used as the working electrode, the reference electrode and the counter electrode, respectively. The working electrode was prepared as follows: firstly, catalyst ink was prepared by adding 5 mg of catalyst in 1 mL the mixture of water and isopropanol ( $v/v=1:1$ ), and 50  $\mu\text{L}$  Nafion solution (5 wt%) was added into the solution, followed by ultrasonication to obtain a homogeneous ink. then an aliquot of 20  $\mu\text{L}$  dispersion was pipetted onto GCE ( $0.196 \text{ cm}^2$ ) and dried at room temperature. The catalyst loading was about  $0.486 \text{ mg}/\text{cm}^2$ . The durability test was performed at a static overpotential for 12 h, during which the current variation with time was recorded.

## **Results And Discussions**

The tubular  $\text{MoP}/\text{MoS}_2$  composite assembled from nanosheets was synthesized by partially phosphating of tubular  $\text{MoS}_2$ . Figure 1a shows the XRD patterns of  $\text{MoP}/\text{MoS}_2$ -1. It is obvious that the diffraction peaks at  $14.1^\circ$ ,  $33.0^\circ$ ,  $39.5^\circ$  and  $58.6^\circ$  are corresponding to (002), (100), (103) and (110) planes of typical  $\text{MoS}_2$  (JCPDS card no. 65-1951), respectively. While the diffraction peaks at  $27.8^\circ$ ,  $32.0^\circ$ ,  $42.9^\circ$ , and  $57.0^\circ$  can be ascribed to the (001), (100), (101), and (110) planes of  $\text{MoP}$  (JCPDS card no. 89-5110), respectively. So it is confirmed that the  $\text{MoP}$  can be successfully produced by the replacement of S atoms with P in  $\text{MoS}_2$ , because they have similar atomic radii. SEM images of  $\text{MoP}/\text{MoS}_2$ -1 are shown in Fig. 1b and c. The hollow tubes are approximately 10  $\mu\text{m}$  in length and 1  $\mu\text{m}$  in width, and the thickness of the wall is approximately 200 nm, which can be observed from the open end of a single tube.

The walls of the hollow tubes are fabricated by loosely stacked nanosheets with the thickness of the nanosheet about 8 nm. It is obvious that the basal planes and the edges of the MoP/MoS<sub>2</sub> composite can be totally exposed to the electrolyte. Compared with the MoS<sub>2</sub> template as shown in Fig. S1a, the tubular structure and the nanosheets were well kept without any damage. The energy-dispersive X-ray (EDX) elemental mapping images of MoP/MoS<sub>2</sub>-1 are displayed in Fig. 1d. It can be observed that the Mo, S, and P elements are distributed homogeneously over the tubular MoP/MoS<sub>2</sub>-1. The hollow tubular structure of MoP/MoS<sub>2</sub>-1 assembled from nanosheets can be further confirmed by TEM images of MoP/MoS<sub>2</sub>-1 with different magnifications in Fig. 1e and f. A distinct heterojunction can be found in the HRTEM image as shown in Fig. 1g. The lattice spacing of 0.63 nm and 0.28 nm can be ascribed to the (002) plane of MoS<sub>2</sub> and the (100) plane of MoP, respectively. The hollow tubular structure of MoP/MoS<sub>2</sub>-1 is favorable for the abundant mass diffusion, the nanosheets can provide active sites and short diffusion path, and the rich heterojunctions between MoS<sub>2</sub> and MoP on the nanosheets may be favorable in promoting the electrocatalytic performance for HER because the migration of electrons become easily [30,31].

X-ray photoelectron spectroscopy (XPS) was conducted to analyze the chemical compositions and states of the MoP/MoS<sub>2</sub>-1. Figure 2a shows the survey XPS spectrum, and it is clear that MoP/MoS<sub>2</sub>-1 comprises Mo, S, and P elements. The XPS spectrum of Mo 3d can be divided into four peaks as shown in Fig. 2b. The peaks at 232.1 and 229.0 eV can be ascribed to the bonding energy of Mo 3d<sub>3/2</sub> and Mo 3d<sub>5/2</sub> of the Mo<sup>4+</sup> [36], respectively. While the peaks at 231.1 and 227.8 eV correspond to the bonding energy of Mo 3d<sub>3/2</sub> and Mo 3d<sub>5/2</sub> of Mo<sup>3+</sup>. Figure 2c shows two distinct peaks at 162.9 and 161.7 eV, which correspond to S 2p<sub>1/2</sub> and 2p<sub>3/2</sub> of MoP/MoS<sub>2</sub>-1, respectively. Figure 2d shows the P 2p spectra of MoP/MoS<sub>2</sub>-1 with two characteristic peaks at 130.0 eV for P 2p<sub>1/2</sub> and 129.1 eV for P 2p<sub>3/2</sub> of P-Mo bonds, respectively. These results further confirm that the coexistence of MoP and MoS<sub>2</sub> in hierarchical tubular MoP/MoS<sub>2</sub>-1.

In order to get the optimal electrocatalyst for HER, a series of composites with different ratios of MoP to MoS<sub>2</sub> were prepared by adjusting the weight ratio of NaH<sub>2</sub>PO<sub>2</sub> to MoS<sub>2</sub>. Figure 3 shows the XRD patterns of MoP/MoS<sub>2</sub>-0, MoP/MoS<sub>2</sub>-1/3, MoP/MoS<sub>2</sub>-5 and MoP/MoS<sub>2</sub>-40. It can be observed that the intensities of the diffraction peaks of MoP become stronger with the increase of the weight ratio of NaH<sub>2</sub>PO<sub>2</sub> to MoS<sub>2</sub>. Especially when the 40 times of NaH<sub>2</sub>PO<sub>2</sub> to MoS<sub>2</sub> was used in the synthesis process, the diffraction peaks of MoS<sub>2</sub> totally disappeared, and only those of MoP can be observed. This result indicates that the ratio of MoP to MoS<sub>2</sub> can be adjusted by simply changing the weight ratio of NaH<sub>2</sub>PO<sub>2</sub> to MoS<sub>2</sub>. The phosphorization degree can be reflected by the intensity ratios of the (100) diffraction plane of the MoP and MoS<sub>2</sub> phase [30], and they are about 0.6, 1.6 and 2.1 for MoP/MoS<sub>2</sub>-1/3, MoP/MoS<sub>2</sub>-1 and MoP/MoS<sub>2</sub>-5, respectively.

The SEM images of the samples were shown in Fig. 4. It is obvious that MoP/MoS<sub>2</sub>-1/3 and MoP/MoS<sub>2</sub>-5 had almost the same tubular structure as MoS<sub>2</sub> with the wall assembled from nanosheets, while the

MoP/MoS<sub>2</sub>-40 was hollow tubes with the wall composed of nanoparticles. Figure S2 and S3 show the homogeneous distribution of Mo, S and P elements over MoP/MoS<sub>2</sub>-1/3 and MoP/MoS<sub>2</sub>-5. While only Mo and P elements can be observed on MoP/MoS<sub>2</sub>-40 (Fig. S4). The EDX results showed that the phosphorus content of the synthesized materials increased with the increase of the mass ratio of NaH<sub>2</sub>PO<sub>2</sub> to MoS<sub>2</sub> (Table S1). Figure 3a shows the survey XPS results of the MoP/MoS<sub>2</sub>-0, MoP/MoS<sub>2</sub>-1/3, MoP/MoS<sub>2</sub>-5 and MoP/MoS<sub>2</sub>-40. For MoP/MoS<sub>2</sub>-0, two peaks at 229.7 and 232.8 eV indicate the chemical state of Mo is +4, and two characteristic peaks at 162.6 eV and 163.6 eV correspond to S. MoP/MoS<sub>2</sub>-1/3 and MoP/MoS<sub>2</sub>-5 showed the similar spectrum with MoP/MoS<sub>2</sub>-1 except for the increase P/S atom ratio as shown in Fig. 3, and the calculated P/S atom ratio are 0.059, 0.088 and 0.114 for MoP/MoS<sub>2</sub>-1/3, MoP/MoS<sub>2</sub>-1 and MoP/MoS<sub>2</sub>-5, respectively. For MoP/MoS<sub>2</sub>-40, the peaks at 231.1 and 227.8 eV correspond to the bonding energy of Mo 3d<sub>3/2</sub> and Mo 3d<sub>5/2</sub> of Mo<sup>3+</sup>, respectively. The peaks at 130.0 eV for P 2p<sub>1/2</sub> and 129.1 eV for P 2p<sub>3/2</sub> of P-Mo bonds, respectively. According to the ratio of Mo<sup>3+</sup> and Mo<sup>4+</sup> in the composites, the ratio of MoP/MoS<sub>2</sub> are calculated to be 0.041, 0.082 and 0.128 for MoP/MoS<sub>2</sub>-1/3, MoP/MoS<sub>2</sub>-1 and MoP/MoS<sub>2</sub>-5, respectively. Both XRD and XPS results confirmed that the increase of the MoP content with the increase of the weight ratio of NaH<sub>2</sub>PO<sub>2</sub> to MoS<sub>2</sub>. The nitrogen sorption isotherm and the pore size distribution curves of the samples are shown in Fig. S5. The BET specific surface area of MoS<sub>2</sub>, MoP/MoS<sub>2</sub>-1/3, MoP/MoS<sub>2</sub>-1, MoP/MoS<sub>2</sub>-5 and MoP/MoS<sub>2</sub>-40 are 9.5, 13.1, 14.3, 14.3 and 7.1 m<sup>2</sup>/g. The higher specific surface area of MoP/MoS<sub>2</sub>-1 and MoP/MoS<sub>2</sub>-5 will provide more active sites for electrochemical reaction.

The HER activities of MoS<sub>2</sub>, MoP and a series of MoP/MoS<sub>2</sub> composites were evaluated in a three-electrode electrochemical cell. As the control, the electrocatalytic performance of Pt/C was tested. Figure 5a shows the polarization curves of the samples in N<sub>2</sub>-saturated 0.5 M H<sub>2</sub>SO<sub>4</sub>. It is obvious that Pt/C displays superior HER electrocatalytic performance with a nearly zero onset potential and a high current density. Compared to other samples, MoS<sub>2</sub> displayed the poorest activity with onset potential of 165 mV (obtained at 1 mA/cm<sup>2</sup>) and an overpotential of 260 mV to obtain a current density of 10 mA/cm<sup>2</sup>. The MoP/MoS<sub>2</sub> composites and MoP displayed better electrochemical performances compared with the tubular MoS<sub>2</sub> as shown in Fig. 5a. The onset potentials are about 71, 37, 51, and 56 mV for MoP/MoS<sub>2</sub>-1/3, MoP/MoS<sub>2</sub>-1 and MoP/MoS<sub>2</sub>-5 and MoP/MoS<sub>2</sub>-40, respectively. Among the catalysts, the activity MoP/MoS<sub>2</sub>-1 exhibited the highest activity for HER with an overpotential of 101 mV to deliver a current density of 10 mA/cm<sup>2</sup>. Though MoP/MoS<sub>2</sub>-1/3 and MoP/MoS<sub>2</sub>-5 are composed of MoP and MoS<sub>2</sub>, their performance for HER were poorer than MoP/MoS<sub>2</sub>-1 as shown in Fig. 5a, which may be ascribed the proper ratio of MoP and MoS<sub>2</sub> in MoP/MoS<sub>2</sub>-1, and similar results have been reported [27,30,31].

Tafel slopes are commonly used to illustrate the inherent properties of the catalyst and reaction kinetic mechanism for HER, which are fitted to Tafel equation  $\eta = b \log j + a$  ( $b$  is the slope and  $j$  is the current density). Figure 5b shows the Tafel slopes of Pt/C and the as-prepared samples, The Tafel slopes of Pt/C was 32 mV/dec, in accordance with reported values [30]. The Tafel slopes of MoP/MoS<sub>2</sub>-0, MoP/MoS<sub>2</sub>-

1/3, MoP/MoS<sub>2</sub>-1, MoP/MoS<sub>2</sub>-5 and MoP/MoS<sub>2</sub>-40 were 84, 64, 56, 64 and 73 mV/dec, respectively. The slope values of the samples are in the range of 50–90 mV/dec which suggests that the HER taking place on the surfaces of the catalysts. MoS<sub>2</sub>, MoP/MoS<sub>2</sub> composites and MoP should undergo the Volmer–Heyrovsky mechanism and the electrochemical desorption is the rate-determining step.

In order to study the intrinsic performance of the synthesized samples, the exchange current density ( $j_0$ ) was obtained by extrapolation from the Tafel plots. As shown in Fig. 5c, the  $j_0$  values are 0.011, 0.083, 0.247, 0.132 and 0.232 mA for MoS<sub>2</sub>, MoP/MoS<sub>2</sub>-1/3, MoP/MoS<sub>2</sub>-1, MoP/MoS<sub>2</sub>-5 and MoP/MoS<sub>2</sub>-40, respectively. It is obvious that MoP/MoS<sub>2</sub>-1 exhibited a higher  $j_0$  than the other samples, which demonstrates the fastest reaction rate per surface area on MoP/MoS<sub>2</sub>-1 electrode. In order to assess the electrochemical activity surface area (ECSA), the double layer capacitance ( $C_{dl}$ ) at the catalyst–electrolyte interface was calculated using cyclic voltammetry plots in a potential range (0.1–0.2 V vs. RHE, in which no faradic reaction was observed) with various scan rates (10 to 60 mV/s). The typical CV curves of the MoP/MoS<sub>2</sub>-1 electrode are shown in Fig. 5d. The calculated double layer capacitance values of the MoP/MoS<sub>2</sub>-0, MoP/MoS<sub>2</sub>-1/3, MoP/MoS<sub>2</sub>-1, MoP/MoS<sub>2</sub>-5 and MoP/MoS<sub>2</sub>-40 were 2.8, 5.7, 7.6, 6.0 and 3.8 mF/cm<sup>2</sup>, respectively (Fig. 5e). The  $C_{dl}$  value of the MoP/MoS<sub>2</sub>-1 electrode is larger than those of the other samples, which indicates MoP/MoS<sub>2</sub>-1 electrode has a large ECSA with rich active sites towards the HER. As a HER catalyst, MoP/MoS<sub>2</sub>-1 outperformed the other as-prepared samples and recently reported molybdenum-based and non-noble-metal catalysts due to its low overpotential and small Tafel slope [18,37-39]. The long-term durability of MoP/MoS<sub>2</sub>-1 is evaluated by the long-term CV cycling and the time dependence of the current density at an overpotential of 100 mV. As shown in inset of Fig. 5f, the polarization curves of MoP/MoS<sub>2</sub>-1 after 500 CV cycles almost overlaps with that before the cycle. Furthermore, the current density slightly declined during the chronoamperometry operation for 12 h in 0.5 M H<sub>2</sub>SO<sub>4</sub> (Fig. 5f). All the above results indicate that the catalyst has good cycle stability.

Generally, the HER activity of the catalyst is closely related to the relative free energies of H\* adsorption on the catalyst ( $\Delta G_{H^*}$ ). So density functional theory (DFT) calculations were conducted to get the adsorption energies of H\* on the surfaces of MoS<sub>2</sub>, MoP/MoS<sub>2</sub> composite and MoP to understand the activity origin of the catalyst. According to Sabatiers' principle, the closer to zero the  $\Delta G_{H^*}$  is, the higher HER activity it will have [40]. Figure 6 shows the geometric models of H\* adsorbed on catalysts. The calculated  $\Delta G_{H^*}$  for H\* adsorption on MoS<sub>2</sub> and MoP are 2.20 eV and -1.15 eV, respectively. While the value for adsorption on MoP/MoS<sub>2</sub> composite is about -0.35 eV. It can be concluded that the more favorable H\* adsorption kinetics on the surface of the MoP/MoS<sub>2</sub> composite during the HER process.

A good catalyst should have excellent HER activity in a wide pH range. To explore the application of the hierarchical tubular MoP/MoS<sub>2</sub>-1 composite under alkaline and neutral conditions, the polarization curves and Tafel plots of the samples were tested in 1 M KOH (Fig. S7 a,b) and 1 M PBS (Fig. S7 c,d). The Tafel slopes of MoP/MoS<sub>2</sub>-1 under alkaline and neutral conditions were 78 and 93 mV/dec, respectively. The current densities of the catalyst can reach 10 mA/cm<sup>2</sup> at overpotential of 210 mV in 1 M KOH and

257 mV in 1 M PBS, respectively. The results demonstrate that hierarchical tubular MoP/MoS<sub>2</sub> composites are promising catalysts for the HER over a broad pH range.

## Conclusion

A series of tubular MoP/MoS<sub>2</sub> composites were synthesized using the tubular MoS<sub>2</sub> as template. As a HER catalyst, MoP/MoS<sub>2</sub>-1 exhibited excellent HER activity with a small overpotential of 101 mV in 0.5 M H<sub>2</sub>SO<sub>4</sub> at current density of 10 mA/cm<sup>2</sup> and a small Tafel slope of 56 mV/dec. The outstanding electrocatalytic activity of MoP/MoS<sub>2</sub>-1 may be benefit from its hierarchical porous structure and abundant MoS<sub>2</sub>/MoP heterojunctions on the nanosheets, which ensure the fast mass transport and electron transfer kinetics for HER. DFT calculation results shows that MoP/MoS<sub>2</sub> composite has more favorable H\* adsorption kinetics during the HER process than pristine MoP and MoS<sub>2</sub>. Both experimental results and the theoretical calculations demonstrate that the tubular hierarchical structure with a MoP/MoS<sub>2</sub> heterojunctions can facilitate reaction kinetics to boost the HER performance. We believe that this work can offer a strategy to design electrocatalysts with high performance for HER applications.

## Declarations

The authors declare that they have no known competing financial interests or personal relationships that could have appeared to influence the work reported in this paper.

## Acknowledgements

This work was supported by Natural Science Foundation of China (21771166), Key Scientific Research Project of Colleges and Universities in Henan Province (19A150011, 21A150058), Center Plain Science and Technology Innovation Talents (194200510013), and Computations were done using National Supercomputing Center in Shenzhen, P. R. China.

## References

1. J. Yu, Y. Dai, Q. He, C. Cheng, Z. Shao, M. Ni, *Appl. Phys. Rev.* **7**, 041304 (2020)
2. J. Zhu, L. Hu, P. Zhao, L. Y. S. Lee, K.-Y. Wong, *Chem. Rev.* **120**, 851-918 (2020)
3. A. Eftekhari, *Int. J. Hydrogen Energy* **42**, 11053-11077 (2017)
4. Y. Zhu, Q. Lin, Y. Zhong, H. A. Tahini, Z. Shao, H. Wang, *Energy & Environmental Science* **13**, 3361-3392 (2020)
5. B. Gao, X. Du, Y. Ma, Y. Li, Y. Li, S. Ding, Z. Song, C. Xiao, *Applied Catalysis B-Environmental* **263**, 117750 (2020)
6. V. Mazanek, C. C. Mayorga-Martinez, D. Bousa, Z. Sofer, M. Pumera, *Nanoscale* **10**, 23149-23156 (2018)
7. J. Zheng, A. Wu, H. Chen, X. Lv, A. Xu, X. Li, *Int. J. Hydrogen Energy* **46**, 2026-2035 (2021)

8. Y. Jiao, H. Yan, R. Wang, X. Wang, X. Zhang, A. Wu, C. Tian, B. Jiang, H. Fu, ACS Appl. Mater. Interfaces **12**, 49596-49606 (2020)
9. S. Lai, C. Lv, S. Chen, P. Lu, X. She, L. Wan, H. Wang, J. Sun, D. Yang, X. Zhao, J. Alloys Compd. **817**, 152727 (2020)
10. Q. Fu, J. Han, X. Wang, P. Xu, T. Yao, J. Zhong, W. Zhong, S. Liu, T. Gao, Z. Zhang, L. Xu, B. Song, Adv. Mater. **32**, 1907818 (2020)
11. H. Thi Anh, C. Bae, S. Lee, M. Kim, J. M. Montero-Moreno, J. H. Park, H. Shin, Chem. Mater. **29**, 7604-7614 (2017)
12. H. Huang, J. Huang, W. Liu, Y. Fang, Y. Liu, ACS Appl. Mater. Interfaces **9**, 39380-39390 (2017)
13. S. Karmakar, R. Sarkar, C. S. Tiwary, P. Kumbhakar, J. Alloys Compd. **844**, 155690 (2020)
14. F. M. Meresht, E. S. Iranizad, A. Zare, A. Bayat, M. N. Liavali, Int. J. Hydrogen Energy **45**, 28696-28705 (2020)
15. T. H. M. Lau, X. Lu, J. Kulhavy, S. Wu, L. Lu, T.-S. Wu, R. Kato, J. S. Foord, Y.-L. Soo, K. Suenaga, T. Shik Chi Edman, Chem. Sci. **9**, 4769-4776 (2018)
16. D. Han, Z. Luo, Y. Li, N. Gao, J. Ge, C. Liu, W. Xing, Appl. Surf. Sci. **529**, 147117 (2020)
17. W. Xu, X. Dong, Y. Wang, N. Zheng, B. Zheng, Q. Lin, Y. Zhao, Chemistryselect **5**, 13603-13608 (2020)
18. Y. Wang, F. Lu, K. Su, N. Zhang, Y. Zhang, M. Wang, X. Wang, Chem. Eng. J. **399**, 126018 (2020)
19. D. Xiao, Q. Ruan, D.-L. Bao, Y. Luo, C. Huang, S. Tang, J. Shen, C. Cheng, P. K. Chu, Small **16**, 2001470 (2020)
20. H. Lu, B. Gao, H. Zhang, X. Fan, L. Zheng, J. Tan, S. Wang, Y. Zhang, Q. Gao, Y. Tang, J Mater. Chem. A **8**, 23265-23273 (2020)
21. H. Jin, X. Liu, Y. Jiao, A. Vasileff, Y. Zheng, S.-Z. Qiao, Nano Energy **53**, 690-697 (2018)
22. X. Zhang, F. Zhou, W. Pan, Y. Liang, R. Wang, Adv. Funct. Mater. **28**, 1804600 (2018)
23. M. D. Sharma, C. Mahala, M. Basu, Inorg. Chem. **59**, 4377-4388 (2020)
24. T. Liu, H. Liu, X. Wu, Y. Niu, B. Feng, W. Li, W. Hu, C. M. Li, Electrochim. Acta **281**, 710-716 (2018)
25. J. Wang, W. Chen, T. Wang, N. Bate, C. Wang, E. Wang, Nano Research **11**, 4535-4548 (2018)
26. Q. Liu, Z. Xue, B. Jia, Q. Liu, K. Liu, Y. Lin, M. Liu, Y. Li, G. Li, Small **16**, 2002482 (2020)
27. Z. Wu, J. Wang, K. Xia, W. Lei, X. Liu, D. Wang, J Mater. Chem. A **6**, 616-622 (2018)
28. J.-Q. Chi, Y.-M. Chai, X. Shang, B. Dong, C.-G. Liu, W. Zhang, Z. Jin, J Mater. Chem. A **6**, 24783-24792 (2018)
29. R. Ye, P. del Angel-Vicente, Y. Liu, M. J. Arellano-Jimenez, Z. Peng, T. Wang, Y. Li, B. I. Yakobson, S. H. Wei, M. J. Yacaman, J. M. Tour, Adv. Mater. **28**, 1427-1432 (2016)
30. A. Wu, C. Tian, H. Yan, Y. Jiao, Q. Yan, G. Yang, H. Fu, Nanoscale **8**, 11052-11059 (2016)
31. A. P. Wu, Y. Gu, Y. Xie, C. G. Tian, H. J. Yan, D. X. Wang, X. M. Zhang, Z. C. Cai, H. G. Fu, ACS Appl. Mater. Interfaces **11**, 25986-25995 (2019)

32. Y. Zou, B. Xiao, J.-W. Shi, H. Hao, D. Ma, Y. Lv, G. Sun, J. Li, Y. Cheng, *Electrochim. Acta* **348**, 136339 (2020)
33. X. Luo, P. Ji, P. Wang, R. Cheng, D. Chen, C. Lin, J. Zhang, J. He, Z. Shi, N. Li, S. Xiao, S. Mu, *Adv. Energy Mater.* **10**, 1903891 (2020)
34. P. Wang, S. Sun, Y. Jiang, Q. Cai, Y.-H. Zhang, L. Zhou, S. Fang, J. Liu, Y. Yu, *ACS Nano* **14**, 15577-15586 (2020)
35. Q. Guan, W. Li, *J. Catal.* **271**, 413-415 (2010)
36. F. Gong, S. Ye, M. Liu, J. Zhang, L. Gong, G. Zeng, E. Meng, P. Su, K. Xie, Y. Zhang, J. Liu, *Nano Energy* **78**, 105284 (2020)
37. B. Vedhanarayanan, J. Shi, J. Y. Lin, S. N. Yun, T. W. Lin, *Chem. Eng. J.* **403**, 126318 (2021)
38. Z. W. Chen, X. Liu, P. J. Xin, H. T. Wang, Y. Wu, C. Y. Gao, Q. Q. He, Y. Jiang, Z. J. Hu, S. S. Huang, *J. Alloys Compd.* **853**, 157352 (2021)
39. X. Y. Peng, C. Huang, B. Zhang, Y. H. Liu, *Int. J. Hydrogen Energy* **45**, 27193-27201 (2020)
40. J. Greeley, T. F. Jaramillo, J. Bonde, I. B. Chorkendorff, J. K. Norskov, *Nat. Mater.* **5**, 909-913 (2006)

## Figures

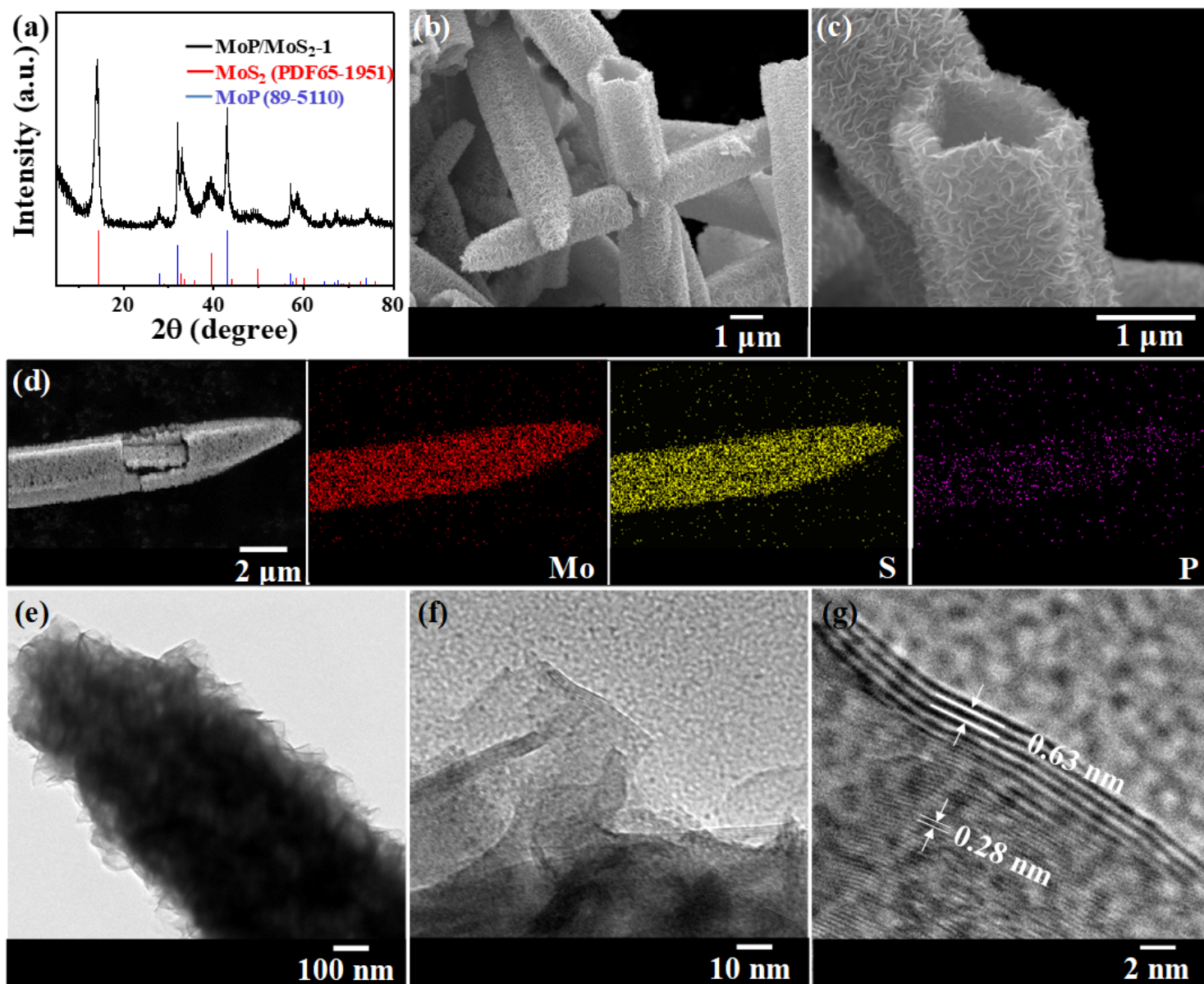


Figure 1

XRD pattern (a); SEM images (b,c); elemental mapping images of Mo, S, and P (d); TEM and HRTEM images (e,f,i) of MoP/MoS<sub>2</sub>-1

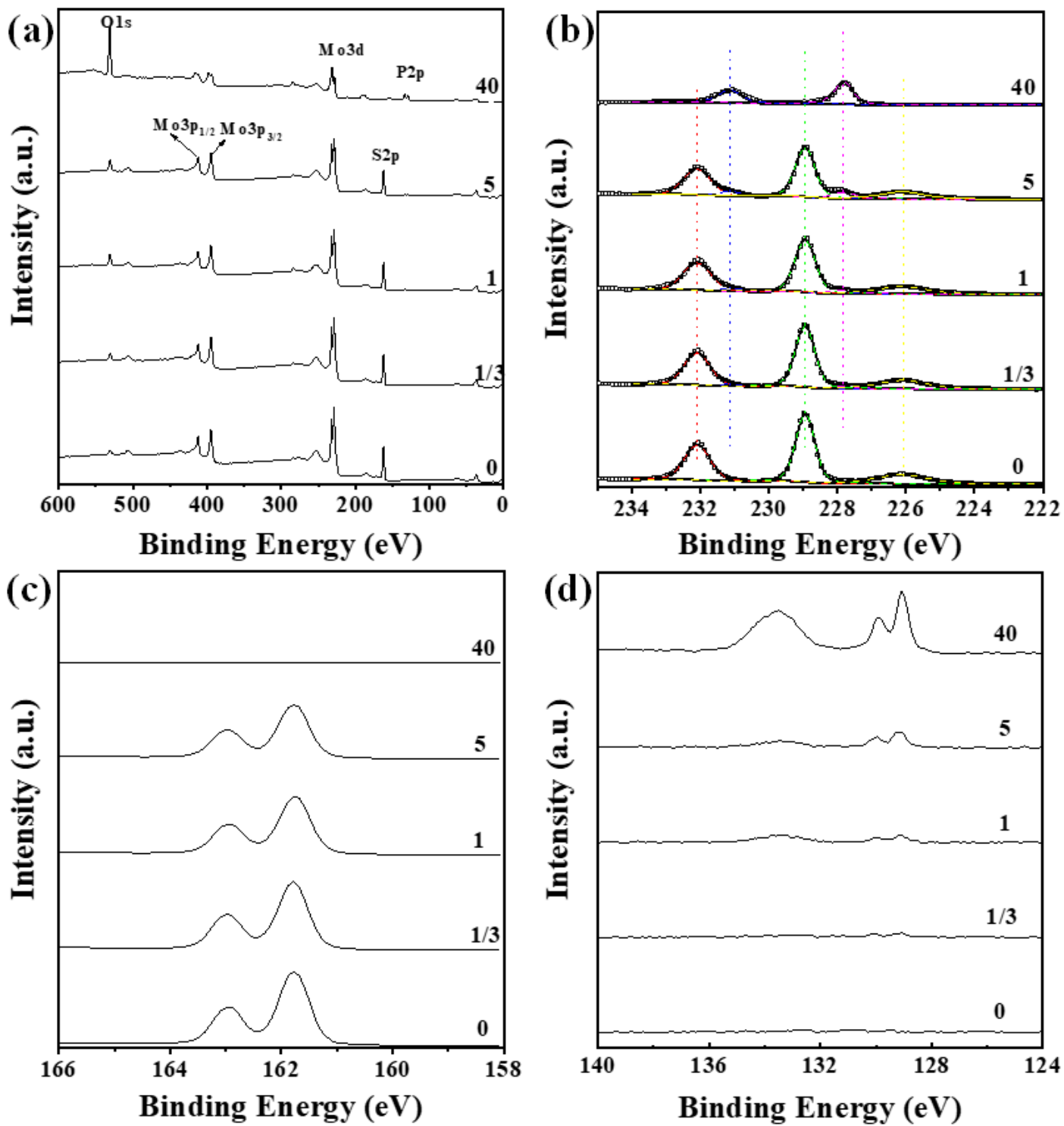


Figure 2

XPS spectra synthesized MoP/MoS<sub>2</sub>: (a) survey spectrum and the high-resolution spectra of (b) Mo 3d, (c) S 2p, and (d) P 2p

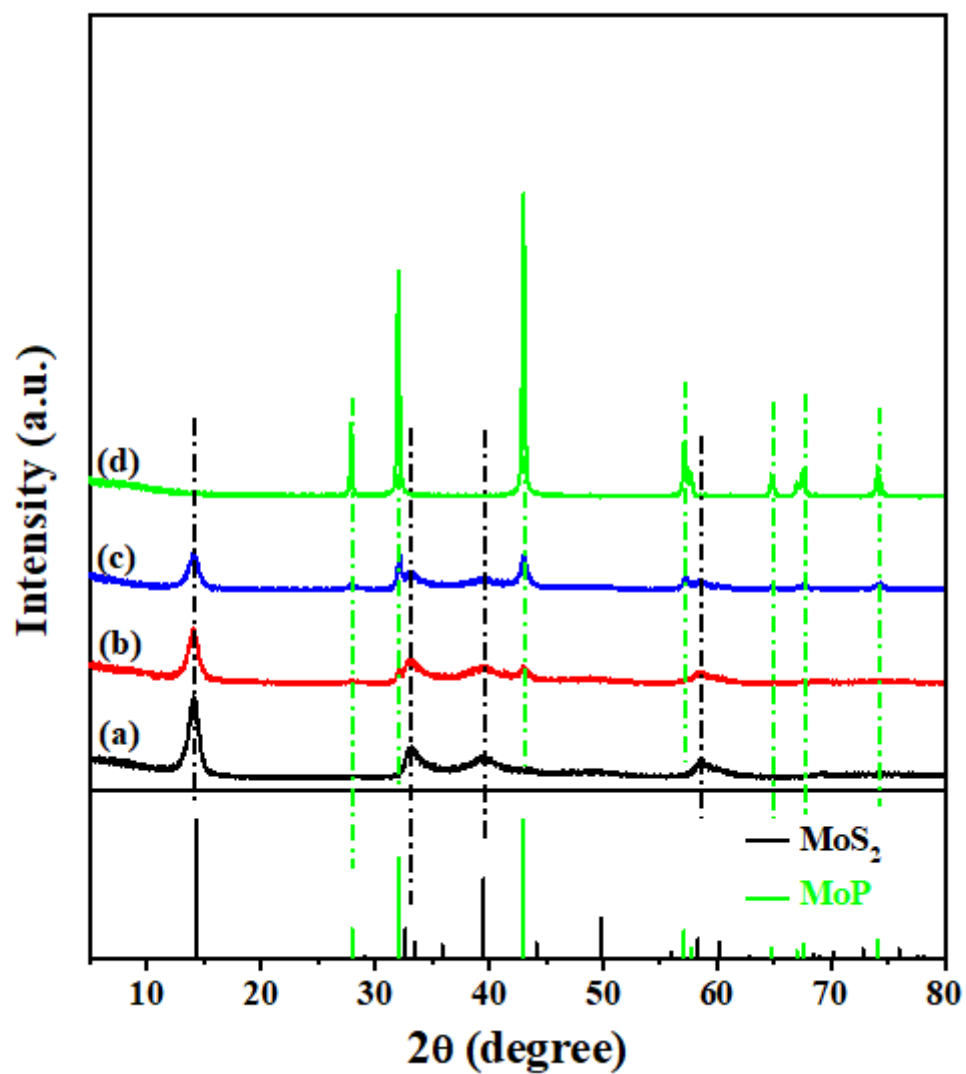
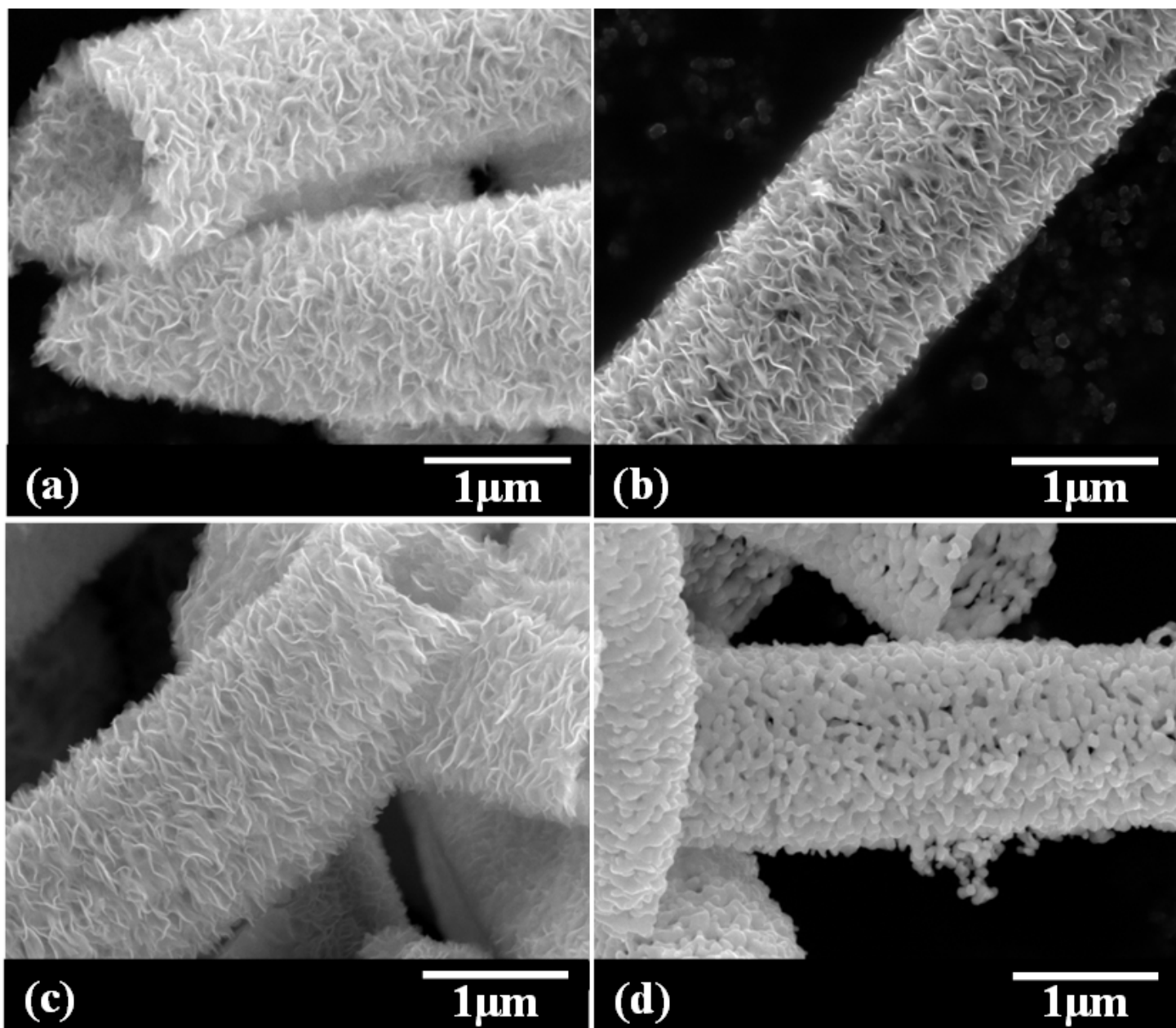


Figure 3

XRD patterns of synthesized MoP/MoS<sub>2</sub>: (a) MoP/MoS<sub>2</sub>-0, (b) MoP/MoS<sub>2</sub>-1/3, (c) MoP/MoS<sub>2</sub>-5, (d) MoP/MoS<sub>2</sub>-40



**Figure 4**

SEM images of synthesized MoP/MoS<sub>2</sub>: (a) MoP/MoS<sub>2</sub>-0, (b) MoP/MoS<sub>2</sub>-1/3, (c) MoP/MoS<sub>2</sub>-5, (d) MoP/MoS<sub>2</sub>-40

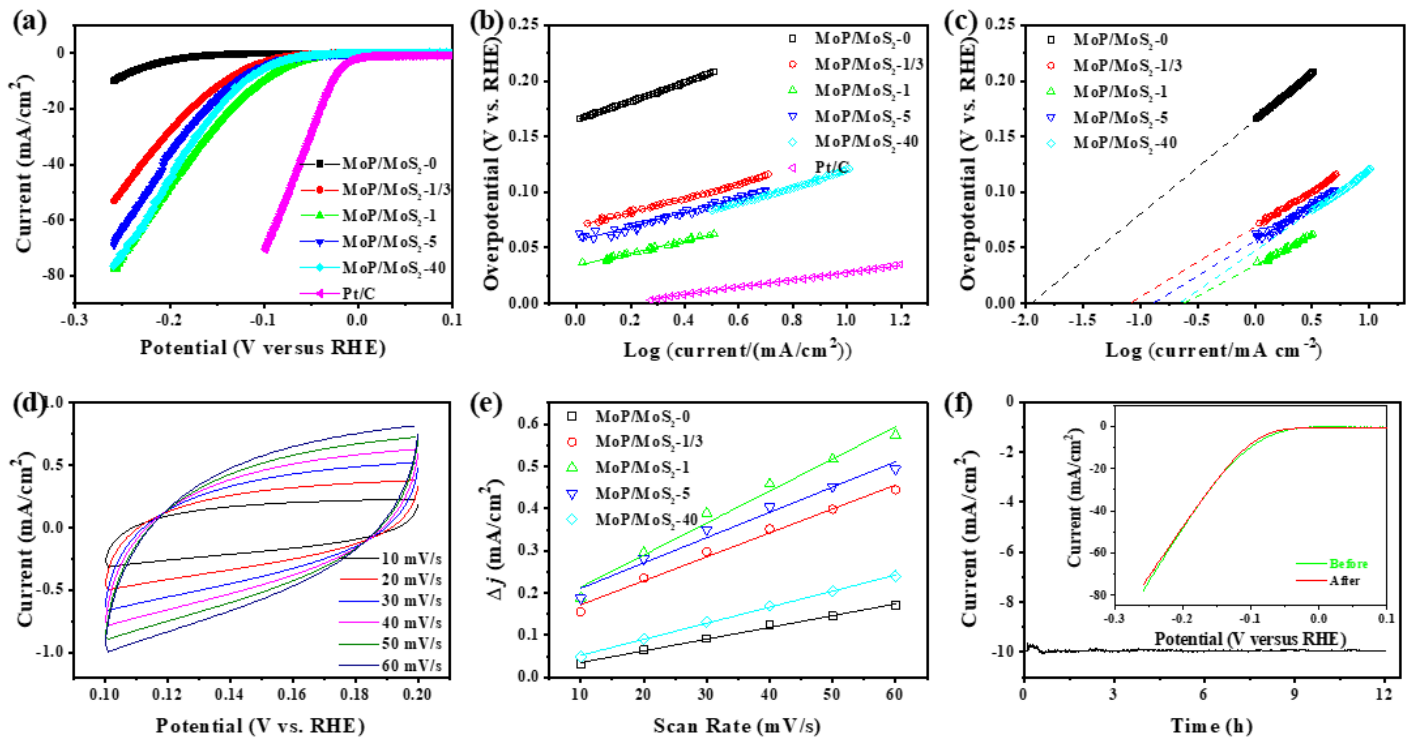


**Figure 5**

Polarization curves (a) of MoP/MoS<sub>2</sub>-0, MoP/MoS<sub>2</sub>-1/3, MoP/MoS<sub>2</sub>-1, MoP/MoS<sub>2</sub>-5, MoP/MoS<sub>2</sub>-40, and Pt/C for HER; Tafel plots (b) of MoP/MoS<sub>2</sub>-0, MoP/MoS<sub>2</sub>-1/3, MoP/MoS<sub>2</sub>-1, MoP/MoS<sub>2</sub>-5, MoP/MoS<sub>2</sub>-40, and Pt/C for HER; Calculation of exchange current density (c) of MoP/MoS<sub>2</sub>-0, MoP/MoS<sub>2</sub>-1/3, MoP/MoS<sub>2</sub>-1, MoP/MoS<sub>2</sub>-5, and MoP/MoS<sub>2</sub>-40 for HER; CVs (d) for MoP/MoS<sub>2</sub>-1 with rates from 10 to 60 mV/s; The capacitive current at 0.15 V as a function of the scan rate (e); Current–time (I–t) curves (f) of MoP/MoS<sub>2</sub>-1 for 12 h, Inset: Polarization curves of MoP/MoS<sub>2</sub>-1 before and after 500 cycles

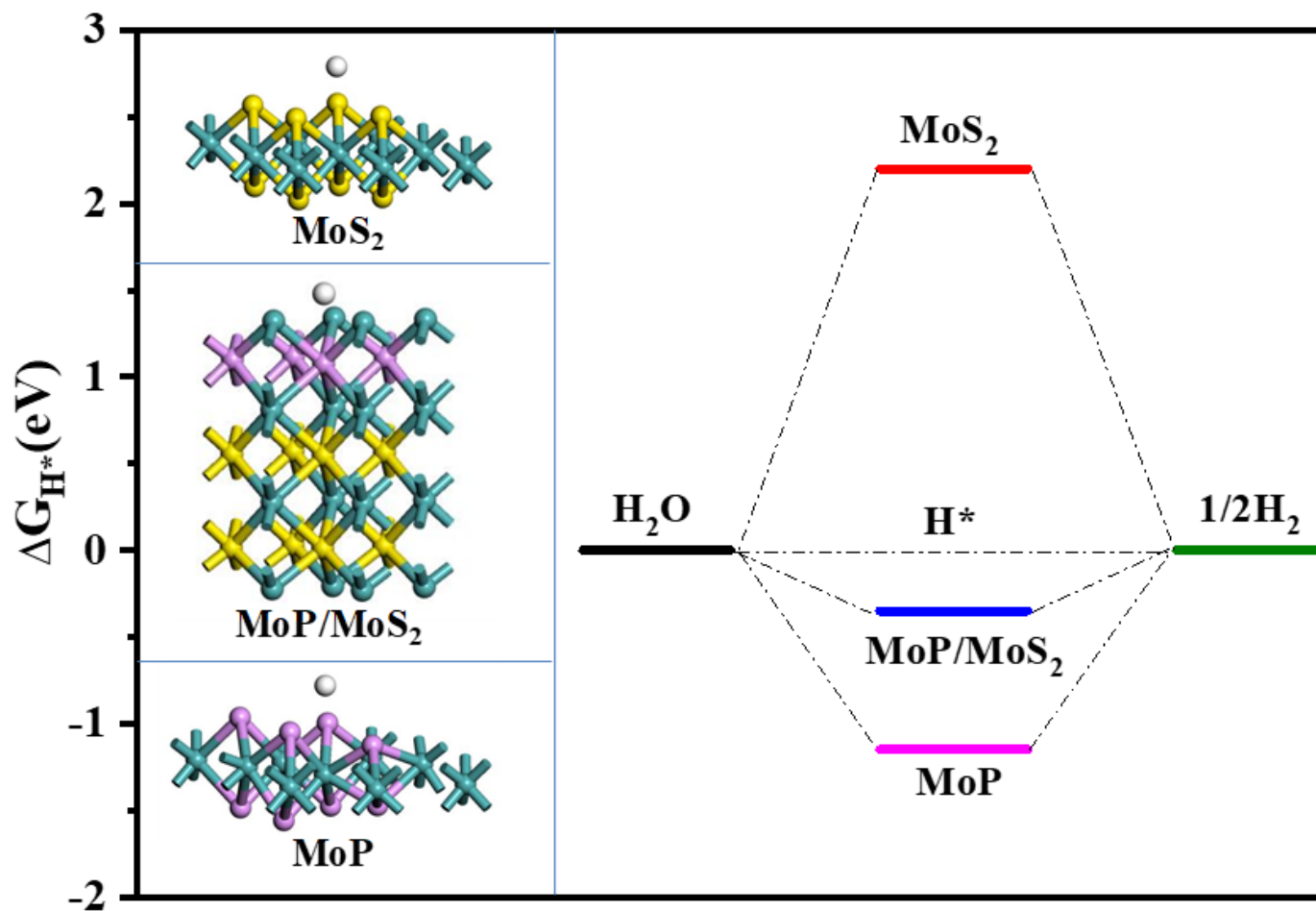


Figure 6

Calculated free energy diagram for the HER on MoS<sub>2</sub>, MoP and MoP/MoS<sub>2</sub> heterostructure

## Supplementary Files

This is a list of supplementary files associated with this preprint. Click to download.

- [Scheme1.png](#)
- [SupportingInformation.docx](#)